machines

MDPI

Article

Systematic Metamodel-Based Optimization Study of Synchronous Reluctance Machine Rotor Barrier Topologies

Branko Ban [1,2,*] and Stjepan Stipetic [1]

[1] Department of Electric Machines, Drives and Automation, Faculty of Electrical Engineering and Computing (FER), University of Zagreb, Unska 3, 10000 Zagreb, Croatia
[2] Torquery Consulting, Blidvädersgatan 56, 41830 Göteborg, Sweden
* Correspondence: branko.ban@fer.hr

Abstract: Nowadays, due to the confidence in modeling tools and rapid product iteration, electric machine designers primarily rely on simulations. This approach reduces time and cost and is very useful when comparing different machine topologies. The prototype stage usually comes after the depletion of all simulation resources. When designing a synchronous reluctance machine, the first step is the selection of rotor barrier type. The literature provides several topologies but does not clearly state which one yields the best performance. The goal of this paper is to determine the best variant for a six-pole machine and the selected requirements using a metamodel-based optimization approach. Seven rotor topologies with different complexities were derived from circular, hyperbolic, and Zhukovsky barrier types (circular concentric, circular variable depth, hyperbolic with fixed eccentricity, hyperbolic with variable eccentricity, original Zhukovsky, modified Zhukovsky variable depth and modified Zhukovsky with equal barrier depth). The novelty of the proposed strategy is in the systematic and fair comparison of different rotor topologies. This approach significantly reduces the total optimization time from several weeks to a few days. Additionally, a novel modified Zhukovsky variable depth topology, which merges the best qualities of all considered variants, was developed. An identical optimization strategy was applied to all variants, and the final results prove that the barrier type substantially affects the final performance of the machine. The best results are achieved by the modified Zhukovsky variable depth topology. In relation to the worst (baseline) topology, the performance gain is 14.9% and the power factor is increased from 0.61 to 0.67. An additional study using different numbers of barrier layers (3, 4, and 5) was conducted to determine the best topology. The best results were achieved with the original four barrier layers.

Keywords: synchronous reluctance; barrier comparison; rotor topology; metamodeling; optimization

Citation: Ban, B.; Stipetic, S. Systematic Metamodel-Based Optimization Study of Synchronous Reluctance Machine Rotor Barrier Topologies. *Machines* **2022**, *10*, 712. https://doi.org/10.3390/machines10080712

Academic Editor: Toomas Vaimann

Received: 1 July 2022
Accepted: 16 August 2022
Published: 19 August 2022

1. Introduction

In recent years, global legislation is stimulating an increase in electric vehicle (EV) production. This has led to a paradigm shift in the automotive industry, forcing the rapid development of propulsion technology, especially in the area of electric traction machines. Due to them having the highest torque and power density compared to other machines, interior rare-earth permanent magnet synchronous machines (IPM) are preferred for automotive traction. Although the performance benefits are undisputed, the use of rare-earth permanent magnet (PM) materials, such as neodymium or dysprosium, has been a commercial risk. This risk can potentially increase as EVs start to penetrate the market on a large scale (Figure 1).

Historically, this has forced some vehicle producers to consider alternative machine designs, which either use no or a minimal amount of rare-earth material. There are notable first-generation passenger vehicles, such as Tesla Model S and Audi e-tron, which use induction machines (IM), and the second-generation Chevrolet Volt, which uses rare-earth-free Ferrite IPM. Currently, there is no commercial use of synchronous reluctance machines

(SyRM) for automotive traction, but due to the cost reduction benefits, they represent a valid alternative [1]. The research presented in [2] provides a theoretical review of major SyRM aspects and highlights potential use niches. The selected application is a commercial vehicle power take-off, an interface that actuates additional body systems, usually powered through variable-speed hydraulic pump (e.g., refuse compressors, hook-lifts, concrete mixers, etc.). In the case of electric vehicles, the interface is referred to as electric power take-off (e-PTO). Considering that the e-PTO needs to be reliable, robust, and cheap, SyRM is the preferred alternative [3,4].

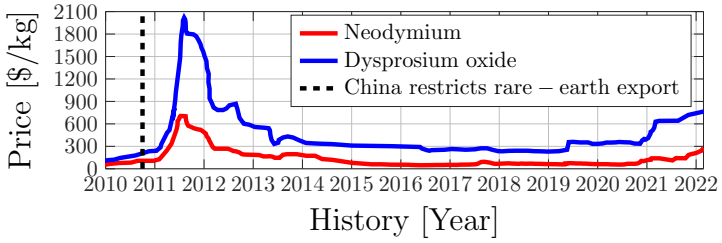

Figure 1. Historical rare-earth material prices.

This paper will concentrate on the e-PTO SyRM design and optimization with requirements carried over from [4]; all terminology is according to Figure 2a.

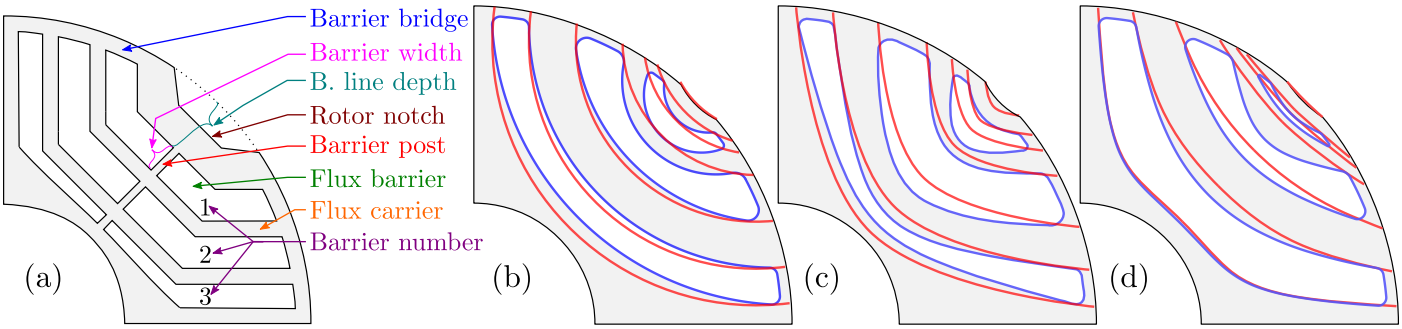

Figure 2. (a) SyRM terminology; SyRM rotor barrier types: (b) Circular variable depth (blue), concentric (red); (c) Hyperbolic variable eccentricity (blue), fixed eccentricity (red); (d) Modified Zhukovsky (blue), original Zhukovsky red;

Most automotive manufacturers have a strategy of reusing components when possible to increase production volume, which leads to price reduction. The presumption is that the e-PTO inverter will have the same part number as a truck traction inverter (i.e., the max power rating for a traction inverter is 180 kW). The obvious conclusion is that the inverter will be oversized for e-PTO application, which effectively eliminates the low power factor issue [4]. Furthermore, the PTO shaft has historically been a part of the diesel engine and has a quite big torque ripple [3,4]. Instead of using torque ripple minimization as an optimization objective, max. ripple was limited to $\leq$15% (a posteriori ripple reduction options were demonstrated through rotor skewing).

Modern electric machine design is strictly tied with some type of multi-objective mathematical optimization workflow. An important milestone in electric machine optimization was the introduction of Differential evolution (DE) algorithm coupled with finite element analysis (FEA) by Lampinen [5]. Further enhancements of the approach were carried out by Žarko et al. [6,7], leading to an overall reduction in optimization time. Current state-of-the-art research projects still heavily depend on similar approaches utilizing different types of optimization algorithms (OAs) such as particle swarm, ant colony, and genetic algorithms [1,8–10]. Although the optimization times are gradually reducing, it is important to note that FEA-based design by means of OA has the serious drawback of a considerable computational burden [9]. This is due to the long FEA simulation time needed to evaluate

a single rotor candidate and the high number of FEA evaluations required by the OA to converge (it can take up to a week until the optimization converges). More details about the typical optimization approach are available in the Section 3.1.

On the other hand, this paper presents a novel, meta-model-based optimization strategy that offers a systematic and fair comparison of different electric machine topologies (Section 3.2). Instead of constantly reiterating and modifying best design variants over generations, the proposed method utilizes meta-modeling (or surrogate modeling) to radically decrease optimization time. Although the method is applicable to any type of electric machine, this paper concentrates on the SyRM e-PTO application. Considering the high number of optimized designs, the approach significantly reduces evaluation time from several weeks to a few days (nine different designs were optimized). Additionally, this study introduces a novel modified Zhukovsky variable depth topology, which merges the best qualities of all considered SyRM rotor variants.

To the best of our knowledge, the currently available literature does not cover the proposed approach applied on SyRM design.

1.1. SyRM Advantages

One advantage of SyRM compared to IM and IPM is the lack of squirrel cage and magnets, which results in reduced material and manufacturing costs. This feature leads to SyRM having minimal rotor losses compared to both alternatives [11], and higher efficiency compared to IM [12]. Furthermore, the SyRM control algorithm is very similar to IPM, meaning that the same drive can be used in both cases. Obviously, there are no issues with demagnetization. Finally, SyRM does not produce back electromotive force, which secures fault tolerance and can simplify the electric vehicle drive train (mechanical disconnect is not required), resulting in a cheaper transmission system.

1.2. SyRM Disadvantages and Potential Solutions

The main disadvantage of SyRM compared to IPM is reduced power and torque density. The situation can be improved by using hairpin stator technology which increases the fill factor [13], or by improvements in rotor design. References [12,14] emphasize the benefits of SyRM design for high-speed operation, resulting in higher efficiency system compared with IPM alternative. Ideally, the rotor should be designed without barrier posts [15], with minimal barrier bridge thickness [9,16]. This will obviously compromise mechanical integrity. Nevertheless, this issue can be solved by the use of "smooth barrier" topologies (e.g., circular, hyperbolic...) with injected epoxy resin [15], and carefully applied barrier corner fillets [9,10,16].

The benefits of barrier corner filleting are illustrated in Figure 3, presenting the mechanical stress distribution maps of identical rotors without and with barrier fillets, calculated on the rotational speed of n = 3000 rpm. The mechanical factor of safety, FOS (the ratio between material yield stress and the maximum calculated stress) of Figure 3a rotor is 0.95 indicating likely failure. The addition of fillets to the rotor structure in Figure 3b increases FOS to 2, indicating normal operation without any mechanical issues.

The next SyRM disadvantage compared to IM and IPM is higher torque ripple. Depending on the application, ripple has to be reduced to an acceptable level which is usually 2–4% for vehicle traction or ≈10% in industrial applications.

A typical a posteriori (post optimization) method for torque ripple reduction is rotor (or stator) skewing. The disadvantage of the approach is the reduction in average torque and increased production cost.

On the other hand, a priori (prior to optimization) ripple reduction methods are: increasing the number of poles, application of barrier corner fillets [10], use of barrier notch (Figure 2a), and use of asymmetric pole designs [17].

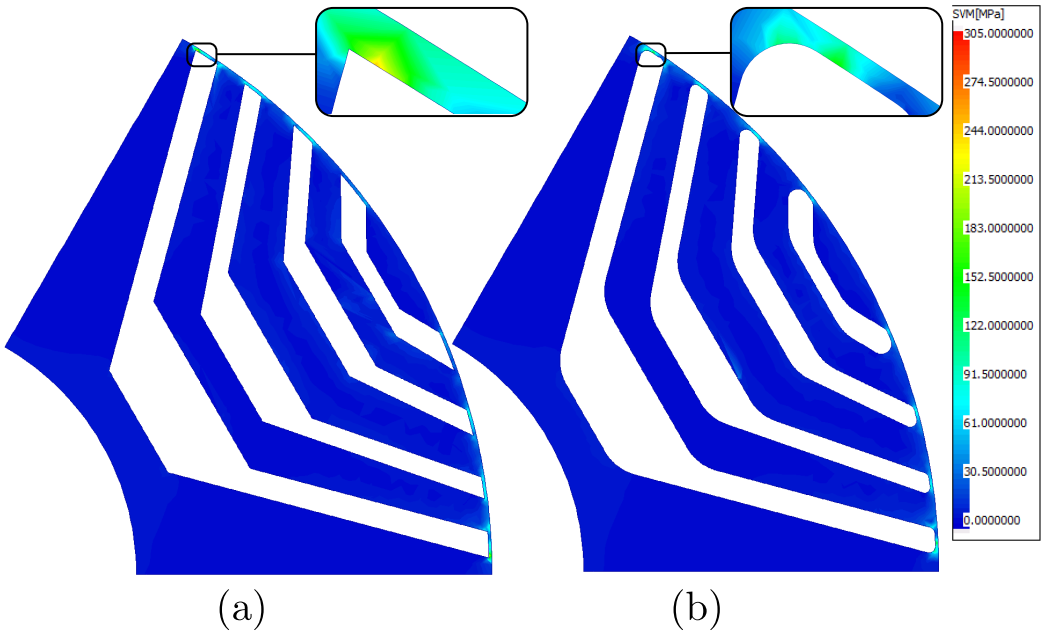

Figure 3. SyRM rotor mechanical stress distribution without (**a**) and with (**b**) barrier fillets.

The function of the barrier notch is to further increase rotor reluctance, otherwise, the flux lines would distribute between adjacent slots thus contributing to the loss of torque and consequently increasing the torque ripple. Detail instructions on slot construction methods are available in [18]. Considering that the high pole number has a strong negative impact on power factor, SyRM machines typically have 4 or 6 poles (more than 6 poles correspond to power factors $\leq$0.6). In case inverter size is not a design constraint, higher pole number combinations can be investigated. Nevertheless, implementation of other a priori methods will effectively reduce torque ripple without major design penalties. Asymmetric pole design is especially interesting because it can significantly reduce torque ripple [19] and potentially eliminate the need for a posterioriskewing, thus making SyRM the cheapest machine variant on the market.

The unavoidable disadvantage of SyRM is the lowest power factor compared to IM and IPM. The only solution to compensate for this drawback is in mass production of inverter switching modules which will enable cheaper technology, with higher current ratings. This will most likely happen when EVs penetrate the market on a large scale.

When it comes to SyRM performance improvements, Tawfiq et. al. [20] stipulate four main areas: rotor optimization, utilization of higher steel grade, winding configuration and inverter control strategies. A great example of SyRM optimization tool-set is provided in Syre platform [21] which additionally enables sensorless controller code generation and the simulation model itself. Winding configuration approaches vary from increasing the number of phases [22,23] to the implementation of delta-star [24], or even concentrated winding [8], all resulting in torque density improvement. Finally, according to [25], the selection of steel grade has a severe impact on SyRM efficiency where the selection of higher grade steel can increase the efficiency by 9%.

2. SyRM Rotor Barriers

The first step in the SyRM design is the selection of rotor barrier type. The literature provides references to several barrier topologies: circular, hyperbolic [26,27], Zhukovsky fluid type [28,29], segmented, etc. The open-source Syre project offers more details and instructions on geometry generation [30]. Currently, the literature does not clearly state which barrier topology yields the best performance. The goal of this paper is to calculate the best topology for the selected requirements within a defined optimization space.

Considering that sharp edges tend to cause mechanical issues, only barrier topologies based on smooth analytical functions have been analyzed (circular, hyperbolic, and

Zhukovsky). Depending on the parametrization, each design variant has a sub-variant. E.g., circular barriers can be concentric or have variable depth, while hyperbolic barriers can have equal or variable eccentricity. On the other hand, the Zhukovsky type cannot be analytically modified to secure variable barrier depth (by definition, Zhukovsky streamlines cannot mutually intersect), in this case, conformal mapping is used to create a modified Zhukovsky barrier type with variable depth lines (barrier construction details for all variants will be covered in the future publications).

Seven barrier topologies have been studied:

1. Circular concentric (CrC), Figure 2b (red);
2. Circular variable depth (CrVD), Figure 2b (blue);
3. Hyperbolic, fixed eccentricity (HyFE), Figure 2c (red);
4. Hyperbolic, variable eccentricity (HyVE), Figure 2c (blue);
5. Original Zhukovsky (Zh), Figure 2d (red);
6. Modified Zhukovsky variable depth (MZhVD), Figure 2d (blue);
7. Modified Zhukovsky with equal depth (MZhED, a special case of previous topology).

2.1. Automated Barrier Design

To simplify, the following figures are drawn for a two and three barrier rotor, the description of all parameters is explained in Tables 3 and 4.

Detailed construction instruction including the pseudo-code is available in [18].

The initial step in rotor construction (Figure 4a) is to specify number of pole pairs (p), rotor barriers (k) and barrier bridge thickness (w_{bb}). The user then specifies dimensionless $\vartheta_{\mathrm{min}}, \vartheta_{\mathrm{max}} \in [0, 1]$ (Table 4, 37–38). Temporary construction points vector $\boldsymbol{E}_{\mathrm{ABC}}$ is then created with equidistant angular spacing ($\Delta\vartheta_r$). Barrier notch point (E_n) is specified with additional parameter $\vartheta_{\mathrm{notch}}$ (Table 4, 39) relative to ϑ_{min} with radial component equal to rotor radius.

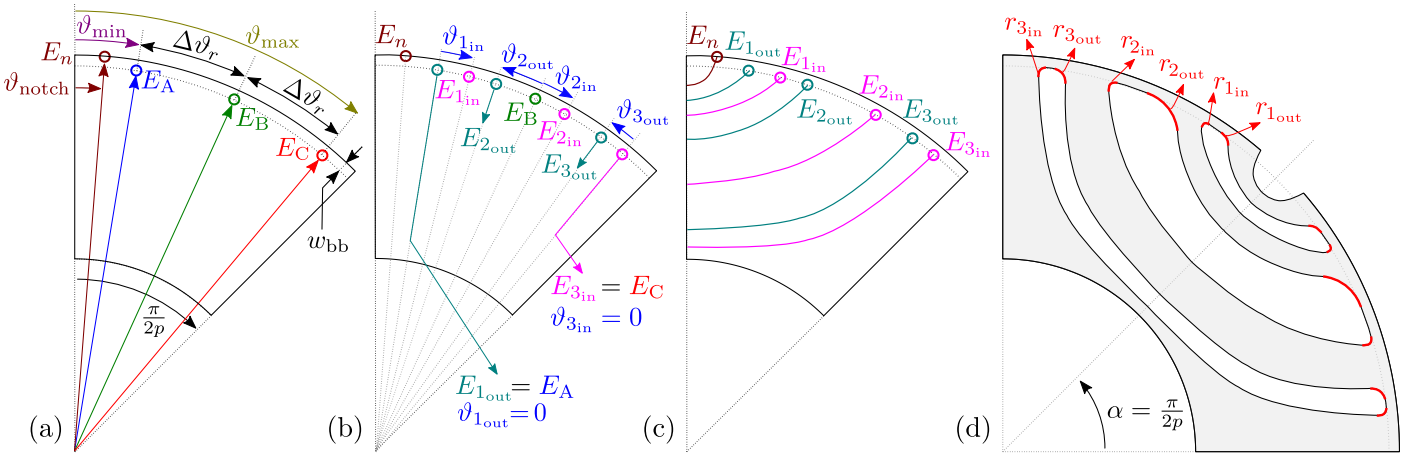

Figure 4. Rotor barrier construction procedure for a three barrier rotor, k=3

The second step (Figure 4b) is the construction of inner and outer barrier line starting points ($\boldsymbol{E}_{1..\mathrm{k\,in}}, \boldsymbol{E}_{1..\mathrm{k\,out}}$). The points are calculated relative to $\boldsymbol{E}_{\mathrm{ABC}}$, based on additional set of dimensionless parameters $\boldsymbol{\vartheta}_{1..\mathrm{k\,in}}, \boldsymbol{\vartheta}_{1..\mathrm{k\,out}} \in [0, 1]$ (Table 4, 15–22).

The last element in barrier line definition is the depth of each line defined by depth parameters $\boldsymbol{D}_{1..\mathrm{k\,in}}, \boldsymbol{D}_{1..\mathrm{k\,out}}, D_n \in [0, 1]$, depending of the barrier type (Figure 4c, Table 4, 41–48).

The final step is the rotation around the center point by the angle $\alpha = \pi/(2p)$ and mirroring the geometry around the half pole axis (Figure 4d). Barrier fillets ($\boldsymbol{r}_{\mathbf{1..}k_{\mathrm{in}}}, \boldsymbol{r}_{\mathbf{1..}k_{\mathrm{out}}} \in [0, 1]$, Table 4, 23–30) responsible for securing mechanical integrity of the rotor are added to the geometry (adding precise fillets to the discrete lines is a complex problem which is planned to be explained in the future publications). The final rotor geometry is exported as *.dxf* to the FEA tool.

2.2. Barrier Depth Variation

The width of the each barrier depends on initial inner and outer line starting points $\boldsymbol{E}_{1..k\,\text{in}}, \boldsymbol{E}_{1..k\,\text{out}}$, and depth coefficients $\boldsymbol{D}_{1..k\,\text{in}}, \boldsymbol{D}_{1..k\,\text{out}}$. Depending on the selected topology, barrier width can be uniform (CrC), approximately uniform (HyFE) or variable (CrVD, HyVE, Zh, MZhED, MZhVD). Considering that the barrier width has a substantial impact on the machine performance, this section will explain how inner and outer barrier depth coefficients affect each of the studied topologies, with a simplified presumption of equal line starting points [18].

In the case of HyFE and CrC, all barrier depths are equal ($\boldsymbol{D}_{1..k\,\text{in}}, \boldsymbol{D}_{1..k\,\text{out}}$). With this simplification, depth variation results in a symmetrical offset that keeps the uniform barrier width (Figure 5a,b). On the other hand, CeVD and HyVE have a higher degree of freedom with unconstrained depth variation resulting in variable barrier width (Figure 5c,d).

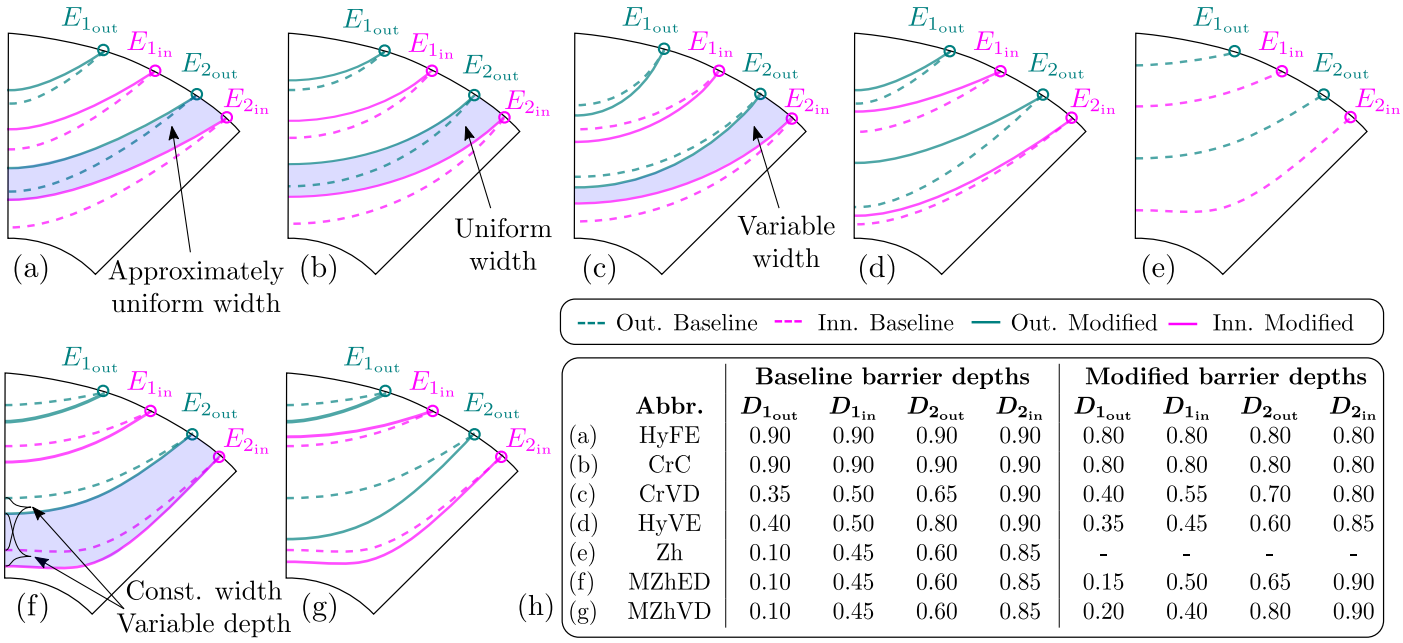

	Abbr.	Baseline barrier depths				Modified barrier depths			
		$\boldsymbol{D}_{1_{\text{out}}}$	$\boldsymbol{D}_{1_{\text{in}}}$	$\boldsymbol{D}_{2_{\text{out}}}$	$\boldsymbol{D}_{2_{\text{in}}}$	$\boldsymbol{D}_{1_{\text{out}}}$	$\boldsymbol{D}_{1_{\text{in}}}$	$\boldsymbol{D}_{2_{\text{out}}}$	$\boldsymbol{D}_{2_{\text{in}}}$
(a)	HyFE	0.90	0.90	0.90	0.90	0.80	0.80	0.80	0.80
(b)	CrC	0.90	0.90	0.90	0.90	0.80	0.80	0.80	0.80
(c)	CrVD	0.35	0.50	0.65	0.90	0.40	0.55	0.70	0.80
(d)	HyVE	0.40	0.50	0.80	0.90	0.35	0.45	0.60	0.85
(e)	Zh	0.10	0.45	0.60	0.85	-	-	-	-
(f)	MZhED	0.10	0.45	0.60	0.85	0.15	0.50	0.65	0.90
(g)	MZhVD	0.10	0.45	0.60	0.85	0.20	0.40	0.80	0.90

Figure 5. Barrier depth variation influence on different 2-barrier (k = 2) SyRM topologies (depth coefficient table is illustrative).

Zh barrier type (Figure 5e) is a special case because it does not support any depth variation. Barrier line depths are defined directly from starting points and cannot be modified. In order to explore the possible benefits of depth variation, Zh type was modified to the following variants. MZhED, where all depths have equal variation, thus achieving symmetrical positive or negative offset (Figure 5f), and MZhVD where barrier depths have full freedom (Figure 5g).

A table of different barrier line depth parameter combinations is provided in Figure 5h. It is important to note that barriers are constructed in such a way that the design is geometrically feasible (there are no barrier intersections of any kind).

2.3. Zhukovsky Barrier Modification

As previously mentioned, Zh lines cannot mutually intersect. To secure barrier depth variability and improve machine performance, we introduce barrier depth modification in complex plain via dimensionless depth parameters $\boldsymbol{D}_{\text{in}}, \boldsymbol{D}_{\text{out}}, D_n$.

Generated rotor barrier lines are defined by sorted vertices containing corresponding $\boldsymbol{x}, \boldsymbol{y}$ coordinates which can be drawn on a 2D real Euclidean plane (Figure 6a). For easier manipulation, real plain coordinates are redefined in complex z-plane ($\boldsymbol{z} = \boldsymbol{x} + j\boldsymbol{y}$), Figure 6b. Considering that the vertices are the same in the real and complex plane, this is a trivial transformation [18].

Electric machine rotors have a circular layout which can be exploited by selecting the convenient complex function $f(z)$ and applying forward conformal mapping to a complex w-plane ($\boldsymbol{w} = \boldsymbol{u} + j\boldsymbol{v}$), Figure 6c. Geometrical modifications of the barrier geometry are then performed in the w-plane and, upon completion, returned back to the z (and real) plane via inverse conformal mapping.

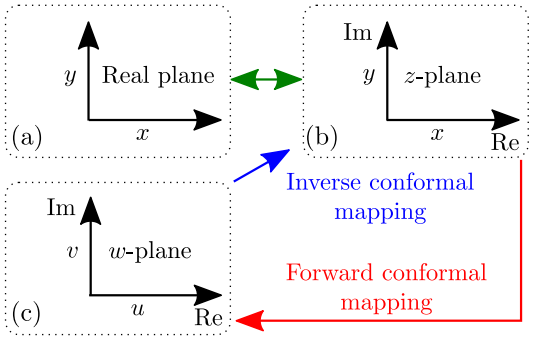

Figure 6. Mapping workflow. Euclidean plane (a); Complex z plane (b); Complex w plane;

Original Zh barrier lines with corresponding $\boldsymbol{x}, \boldsymbol{y}$ vertices are written as $\boldsymbol{z} = \boldsymbol{x} + j\boldsymbol{y}$ (Figure 7a, red) and conformally transformed to w-plane via $w = \ln z$ complex function as $\boldsymbol{w} = \boldsymbol{u} + j\boldsymbol{v}$ (Figure 7b, red).

Upon modification (Figure 7b, blue), barrier lines are mapped back to z-plane via inverse complex function $z = e^w$ (Figure 7a, blue). The main benefit of the approach is easier barrier modification in the w-plane which leads to simplified software coding.

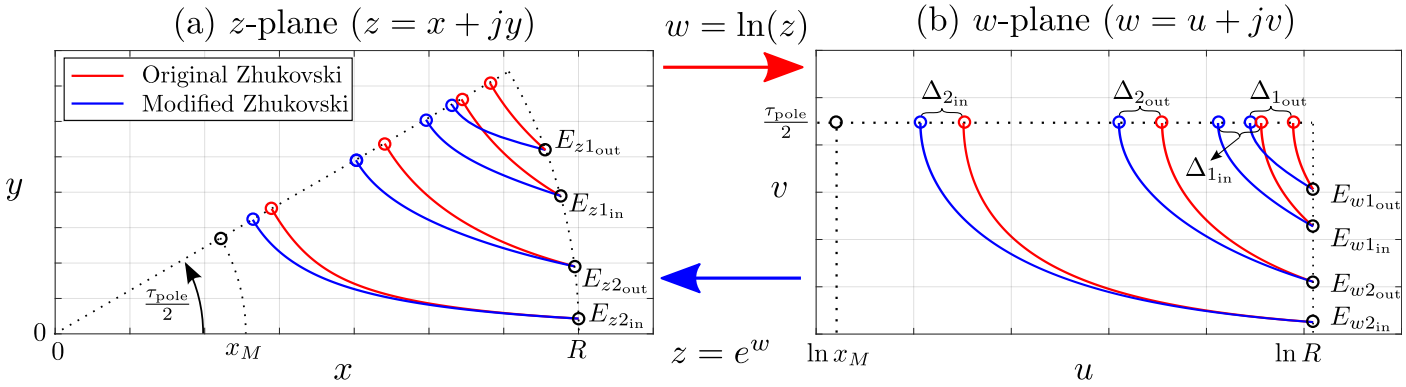

Figure 7. Modification of Zhukovsky lines via conformal mapping.

3. Optimization

3.1. Typical Optimization pProcedure

Most of the electric machine design goals are in conflict with each other and thus form a multi-objective problem (e.g., reduction in volume and mass while increasing the efficiency). When used in EVs, an increased machine weight contributes to the driving range reduction, while a larger volume creates issues with mechanical integration within the drivetrain. Obviously, an optimal trade-off between conflicting requirements is a design imperative. Considering a large number of coupled parameters that affect the final design, manual design is usually not an option. Nowadays, mathematical optimization is used for obtaining better designs.

Optimization algorithms (OAs) can be divided into gradient-based methods and stochastic (metaheuristic) methods. Gradient methods converge fast but have difficulties with global optima because they require a feasible starting point, which can be a problematic task in complex problems [31]. Stochastic methods are heavily used in electrical machine optimization [31]. The drawback is that the convergence can last for days, and the global optimum cannot be mathematically proven. Additionally, some popular metaheuristic

methods are based on natural behavior (Genetic algorithm (GA) [32], Differential evolution (DE) [5], Particle swarm, but they can also be iterative [33], or based on approximation [34]. From an engineering standpoint, both approaches can find a satisfying result.

IPM and SyRM design is highly affected by the saturation within the rotor structure which implies the use of computationally intensive FEA. A typical optimization system consists of the FEA tool (e.g., Ansys Motor-CAD), OA (e.g., DE), and external software, which handles model building and FEA tool communication (e.g., Matlab). When using this (or similar) system, the user has to initially specify all design boundaries and parameters (including upper and lower bounds). OA then generates a set of optimization parameters that define an optimization candidate (a complete machine model). After calculation, FEA results are returned to the OA for evaluation. OA then generates a new population of optimization parameters, repeats the procedure, and propagates through generations until reaching the optimal machine model (Figure 8, color coding according to the used system elements).

According to [32], the GA and the DE are the most preferred OAs, because both algorithms provide fast and accurate solutions for multi-objective problems and they can be run without any need for experimental data. The obvious drawback is that OA requires thousands of design evaluations for proper parameter propagation, which can substantially increase optimization time e.g., DE algorithm took 27500 FEA evaluations and lasted 7 days [4].

The alternative is topology optimization, which can potentially generate novel structures unrelated to traditional, smooth-shape SyRM barriers. The method applies the on/off method based on the normalized Gaussian network (NGnet) [35]; e.g., the algorithm sets the rotor quadrants to consist of either steel or air. However, when using this method, it is difficult to obtain thin-layered flux barriers that are easy to manufacture and can withstand mechanical stresses.

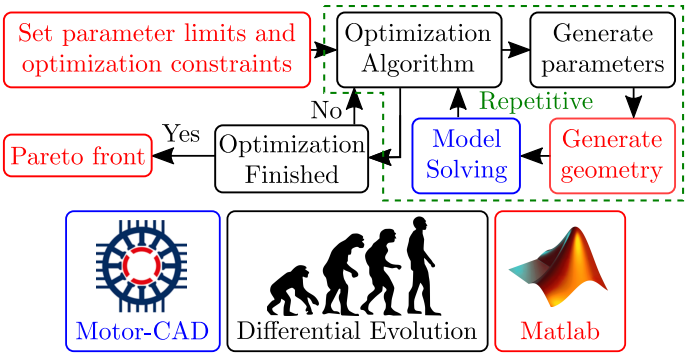

Figure 8. Typical optimization workflow.

The final approach is to use a metamodel (also refereed as surrogate modeling by [36]) based optimization strategy, e.g., Adaptive-Sampling Kriging Algorithm (ASKA), [37]. The ASKA applies kriging interpolation of sampled objective function model which has lower computation time compared with a standard approach. Nevertheless, the accuracy is determined by the sampling quality and objective function complexity. This paper uses a dedicated optimization tool Ansys Optislang (OSL) which combines the standard procedure (OA + FEA tool + external software) with advanced sensitivity analysis and metamodeling, Figure 9.

The additional functionality enables motor designers to leverage the design space and most importantly reduce optimization time [38] (typical optimization time is 2–3 days).

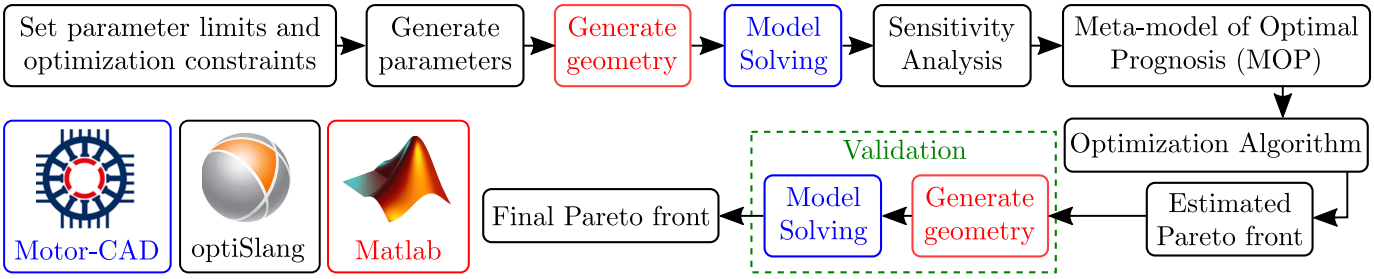

Figure 9. Optimization workflow with Matlab scripting and Motor-CAD FEA tool within Optislang environment.

3.2. OptiSlang Optimization Details

The logic of the OSL tool process is outlined in Figure 9. First, the user has to initially specify all design parameters (including upper and lower bounds) and a number of designs ($N_{\mathrm{Dsg}} = 300$) for initial evaluation. OSL then generates parameters (scans the multidimensional space with a specified sampling method), calls Matlab script which generates electric machine model, and runs FEA calculation for each of the N_{Dsg} designs. Once the variation study has been completed, OSL runs the sensitivity analysis of output parameters in relation to input parameters. Next, OSL creates the so-called metamodels of Optimal Prognosis (MOPs), showing the relationships between performance outputs and design input variables.

The following example highlights the connection between sensitivity analysis and a single MOP (in reality, a model has multiple MOPs created for crucial optimization responses).

In Figure 10, the importance of all input variables is quantified using a variance-based measure called single Coefficient of Prognosis (CoP). The full model CoP (or total CoP) value written at the top of the figure is a crucial measure that is used to assess the forecast quality of the meta-model. This value is always lower than or equal to 100%. The higher this value, the more accurate the MOP prediction. In Figure 11, the torque output MOP is plotted against the two most important parameters, namely the split ratio and stack length. The CoP and MOP approach is used for modeling each critical design response listed in Section 3.4.

The user then selects the preferred optimization algorithm which is applied directly to the MOP with user-specified optimization goals and inequality constraints. The key point here is that the metamodel evaluates almost instantly since it is a mathematical function, instead of a computationally intensive FEA calculation. For multi-objective problems, the best designs from the solution space can be interpreted with the use of a Pareto front. Finally, the number of the MOP-based estimated optimization results (N_{Par}) are validated and verified by running FEA software. Differences may emerge depending on the quality of the calculated MOPs. In that case, the user can either add design samples to the sensitivity analysis or tweak the optimization constraints to increase MOP quality.

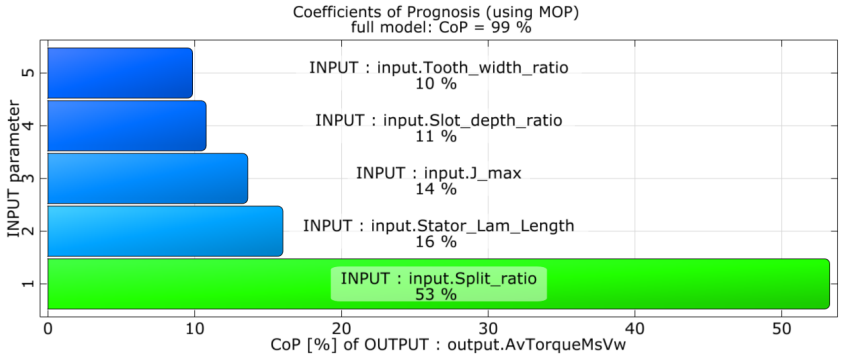

Figure 10. Example of torque response coefficient of prognosis.

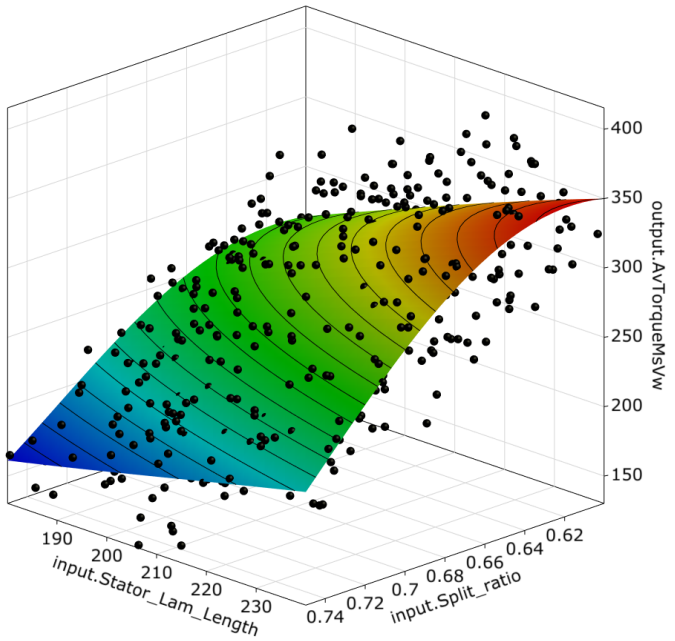

Figure 11. Example of torque response MOP (black dots are the sampling data calculated during the sensitivity analysis).

The strong points of this strategy are:

1. Instead of several thousands, OSL runs only $N_{\mathrm{Dsg}} + N_{\mathrm{Par}}$ FEA calls;
2. Once sensitivity analysis is completed on N_{Dsg}, the user sets objectives, constraints and runs a fast GA optimization procedure (N_{Par} FEA calls). In case some of the goals and constraints have to be modified, sensitivity analysis does not have to be repeated. The user only re-runs optimization and validates it on N_{Par} FEA calls. This is very handy for projects with fluid requirements (e.g., change of rated battery voltage, driving cycle, peak power requirement etc.);
3. Thousands of designs can be evaluated through MOPs within minutes by the selected optimization algorithm;
4. Sensitivity analysis gives a valuable insight into where to concentrate the efforts for specified motor requirements [38].

3.3. Performance Requirements

The requirements for e-PTO machine are derived from [4] and listed in Table 1.

Table 1. Peak operation requirements at base speed.

Description	Symbol	Value	Unit
Base speed	n_b	1700	rpm
Max. operating speed	$n_{\max}$	2500	rpm
Max. torque	$T_{\max}$	$\geq$200	Nm
Battery voltage	U_{DC}	610	V
Max. phase current	$I_{\mathrm{s\,max}}$	300	A_{rms}

3.4. Optimization Objectives and Inequality Constraints

The optimization of the 2D cross-section is set up as a multi-objective problem which is mathematically defined as: find the vector of Parameters (1), subject to D parameter boundary Constraints (2) and subject to m inequality constraints Function (3), which will minimize (or maximize) n objective Function (4).

$$\vec{x} = [x_1, x_2, \ldots, x_D], \quad \vec{x} \in R^D \tag{1}$$

$$x_i^{(L)} \leq x_i \leq x_i^{(U)}, \quad i = 1, \ldots, D \tag{2}$$

$$g_j(\vec{x}) \leq 0, \quad j = 1, \ldots, m \tag{3}$$

$$f_k(\vec{x}) \leq 0, \quad k = 1, \ldots, n \tag{4}$$

Inequality constraints usually arise from various electromagnetic, thermal, mechanical, manufacturing, economic or normative limits such as maximum winding temperature, maximum rotor stress, minimum magnet dimensions, maximum active material cost, maximum noise, etc.

Inequality constraints (Table 2) are taken into consideration in the optimization algorithm box in Figure 9. The constraint function g_1 checks rotor structural factor of safety at maximum over-speed ($1.2 \cdot n_{\max}$). Next, the procedure contains several subfunctions designed according to ultra-fast scaling laws [39]. Multiple magnetostatic FEA calculations are performed to find the optimal maximum torque-per-ampere (MTPA) control angle. The number of turns per coil and the number of parallel paths of the machine is then matched to the required base speed. Constraint g_2 checks the losses are within limits. g_3 and g_4 check that maximum stator yoke and tooth flux density are below limits (the purpose is to penalize the designs with increased iron losses). Constraint g_5 is related to thermal loading coefficient (THL) which is equal to current density multiplied by electrical loading (THL $= J \cdot A$). THL indicates if the machine can be cooled down at specified peak performance. The empirical values indicate that water cooling is possible if THL $\leq$ 1.9 $\mathrm{MA^2/m^3}$.

Finally, a transient FEA calculation is performed at base speed. The transient is performed for the machine without skewing. To fulfill g_6, the calculated TPV must be higher than the limit. If the torque ripple (T_{ripp}) is higher than the limit, the machine does not satisfy the constraint g_7.

The optimization algorithm generates the designs, and the variants which fulfill all inequality constraints populate the estimated Pareto front (optimization goals according to Table 2). The final step is the validation of the estimated Pareto front which completes the optimization process.

Table 2. Inequality constraints and optimization goals.

No:	Constraint Description	Symbol	Limit
g_1	Stress yield factor at $1.2 \cdot n_{\max}$	FOS	$\geq$2
g_2	Total loss	P_{loss}	$\leq$6000 W
g_3	Flux density in stator yoke	$B_{\mathrm{sy,max}}$	$\leq$1.6 T
g_4	Flux density in stator tooth	$B_{\mathrm{st,max}}$	$\leq$1.9 T
g_5	Thermal loading $J \cdot A$	THL	$\leq$1.9 $\mathrm{MA^2/m^3}$
g_6	Torque per volume	TPV	$\geq$25 $\mathrm{Nm/dm^3}$
g_7	Torque ripple without skewing	T_{ripp}	$\leq$15%
No:	**Optimization Goals**	**Symbol**	**Unit**
f_1	Minimize total loss	P_{loss}	W
f_2	Maximize torque per rotor volume	TPV	$\mathrm{Nm/dm^3}$

3.5. Preset Model

Although four poles are a usual choice due to the higher power factor, we selected a six-pole machine. The reason is the higher theoretical torque density and lower torque ripple. In e-PTO application, the lower power factor is not an issue due to the use of an oversized inverter [4]. The number of slots is 54 with 4 rotor flux barriers, resulting in a two-layer integer slot distributed winding. This combination provides a good compromise between the inherent ability to mitigate torque pulsations, susceptibility to noise, and the ability to

use multiple parallel paths. The ideal number of turns per coil (N_c) and parallel paths (a_p) for matching the base speed is automatically calculated based on winding feasibility and ultra-fast scaling laws [39].

All seven topology variants have been optimized in Ansys Optislang. The initial sensitivity study used for MOP building was performed on $N_{\mathrm{Dsg}} = 300$ models per topology. Optimization was conducted using the inbuilt OSL Evolutionary algorithm.

Table 3 lists constant parameters which are equal for all topologies (No. 1–14). The optimization variable range (design space) was initially determined based on the empirical data from the previous projects. A dummy sensitivity analysis was then conducted for fine-tuning any problematic parameter(s). The final optimization variables and respective optimization ranges for each topology (No. 15–49, color coding according to Figure 4) are listed in Table 4.

Table 3. List of constant design parameters.

No:	Description	Symbol	Value/Range	Unit
1	Stator diameter	D_s	214	mm
2	Shaft diameter	D_{sh}	54	mm
3	Phase number	N_{ph}	3	-
4	No. of turns	N_c	Automatic	-
5	Parallel paths	a_p	Automatic	-
6	Coil throw	y_c	9	-
7	Barrier number	k	4	-
8	Pole pairs	p	3	-
9	Slot number	N_s	54	-
10	Barrier bridge	w_{bb}	0.3	mm
11	Airgap	δ	0.7	mm
12	Slot opening	w_{op}	2	mm
13	Fill factor	-	0.43	-
14	Tooth tip depth	d_t	0.5	mm

Table 4. List of optimization variables.

No:	Description	Symbol	Value/Range	Unit
15	Point_1 inner angle	$\vartheta_{1_{\mathrm{in}}}$	[0.22 , 0.47]	-
16	Point_1 outer angle	$\vartheta_{1_{\mathrm{out}}}$	0	-
17	Point_2 inner angle	$\vartheta_{2_{\mathrm{in}}}$	[−0.08 , 0.46]	-
18	Point_2 outer angle	$\vartheta_{2_{\mathrm{out}}}$	[−0.06 , 0.16]	-
19	Point_3 inner angle	$\vartheta_{3_{\mathrm{in}}}$	[0.06 , 0.25]	-
20	Point_3 outer angle	$\vartheta_{3_{\mathrm{out}}}$	[0.09 , 0.11]	-
21	Point_4 inner angle	$\vartheta_{4_{\mathrm{in}}}$	0	-
22	Point_4 outer angle	$\vartheta_{4_{\mathrm{out}}}$	[0.32 , 0.35]	-
23–26	Corner radius in	$r_{1..k_{\mathrm{in}}}$	[0 , 1]	-
27–30	Corner radius out	$r_{1..k_{\mathrm{out}}}$	[0 , 1]	-
31	Slot corner radius	r_{sc}	[0 , 1]	-
32	Slot depth ratio	$\frac{D_s - D_b}{2}$	[0.45 , 0.6]	-
33	Split ratio	D_s / D_b	[0.6 , 0.75]	-
34	Active length	l_{s}	[180 , 240]	mm
35	Tooth tip angle	α_t	[5 , 40]	○
36	Tooth width ratio	$\frac{D_b \pi}{N_s} - w_{op}$	[0.7 , 0.9]	-
37	Min. angle	ϑ_{min}	[0.15 , 0.3]	-
38	Max. angle	ϑ_{max}	[0.9 , 0.95]	-
39	Notch angle	ϑ_{n}	[0.1 , 1]	-
40	Current density	J	[17 , 22]	$\mathrm{A/mm^2}$
41–44	Barrier depths	$D_{1..k_{\mathrm{in}}}$	[0.2 , 1]	-
45–48	Barrier depths	$D_{1..k_{\mathrm{out}}}$	[0.2 , 1]	-
49	Notch depth	D_n	[0 , 1]	-

4. Optimization Results

4.1. Rotor Topology Selection

Figure 12 contains the validated Pareto fronts which fulfil all inequality constraints. For easier comparison, seven designs (one per topology) with approximately the same losses (5200 W) have been selected. Table 5 summarizes the performance of each design at base speed and MTPA conditions from the worst (left) to the best topology (right). All optimized cross-sections are shown in Figure 14, while Table 6 list optimized variables for each design.

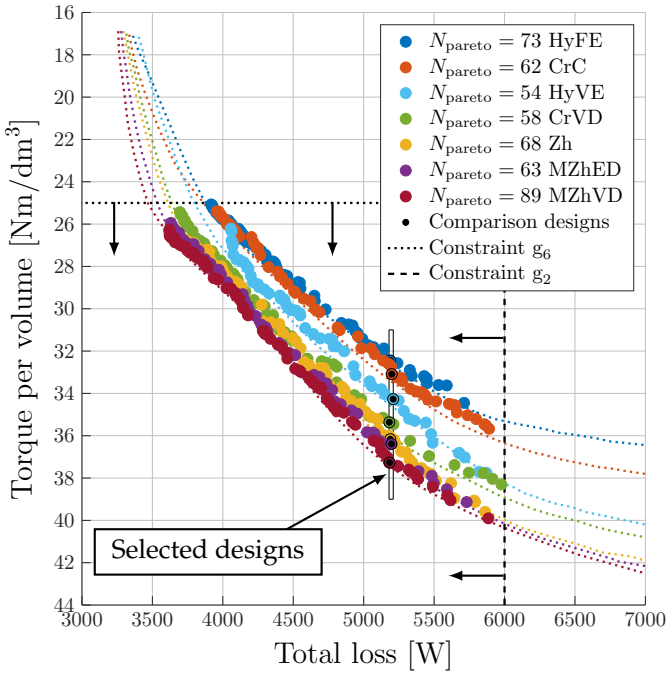

Figure 12. Validated Pareto front within constraints g_2 and g_6. Dotted colored lines represent estimated Pareto fronts. N_{pareto} is the number of designs placed on each front.

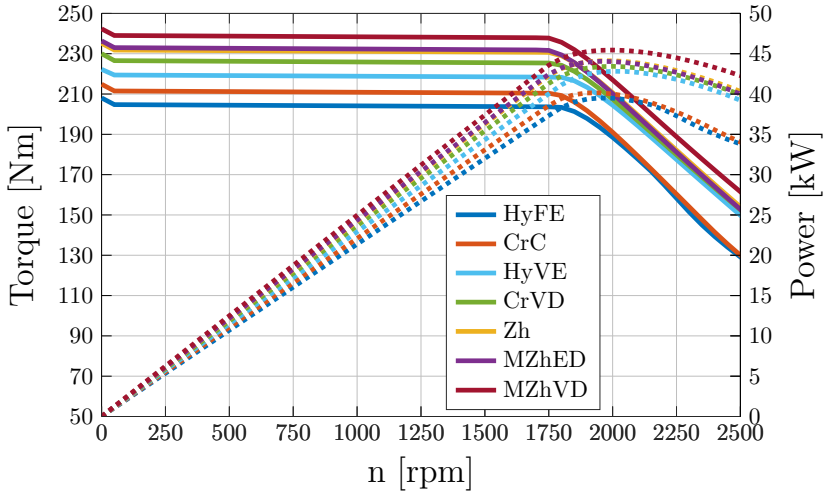

Figure 13. Performance curves of selected designs (Table 5).

Table 5. Final result comparison table.

Name	Unit	HyFE	CrC	HyVE	CrVD	Zh	MZhED	MZhVD
TPV	Nm/dm^3	32.5	33.1	34.3	35.4	36.2	36.4	37.3
V_{active}	dm^3	6.47	6.47	6.47	6.47	6.47	6.47	6.47
P_{loss}	kW	5188	5199	5209	5182	5188	5197	5184
P_{mech}	kW	37.4	38.1	39.5	40.8	41.7	41.9	43.0
T_{avg}	Nm	210.1	214.2	221.9	229.0	234.1	235.6	241.3
$T_{ripp.}$	%	12.1	14.1	11.7	12.7	9.7	9.3	13.7
n	rpm	1700	1700	1700	1700	1700	1700	1700
$B_{sy,max}$	T	1.53	1.53	1.39	1.60	1.52	1.54	1.56
$B_{st,max}$	T	1.86	1.87	1.87	1.82	1.87	1.86	1.84
FOS	-	8.8	9.4	7.3	6.3	3.6	5.2	6.3
m	kg	45.6	46.0	44.2	44.3	45.0	44.8	44.1
THL	MA^2/m^3	1.52	1.53	1.57	1.47	1.53	1.52	1.52
l_s	mm	180	180	180	180	180	180	180
γ	○	57.9	60.3	61.4	62.5	61.8	61.8	62.9
I_{max}	A_{rms}	95.6	95.6	94.3	94.1	95.9	95.7	95.7
$\cos\varphi$	-	0.61	0.62	0.66	0.67	0.67	0.67	0.69
η	%	87.8	88.0	88.3	88.7	88.9	89.0	89.2
Gain	%	0.0	1.9	5.6	9.0	11.4	12.1	14.9

Performance wise, HyFE topology yields the worst results (TPV = 32.5 Nm/dm^3, $\cos\varphi = 0.61$) and will be considered the baseline design (Gain = 0%). Performance gain is calculated via: Gain $= (T_{avg}/T_{HyFE\ avg} - 1) \cdot 100\%$.

CrC topology is slightly better (2% gain) but still has rather low power factor (TPV = 33.1 Nm/dm^3, $\cos\varphi = 0.62$). Next, HyVE yields better results (TPV = 34.3 Nm/dm^3, $\cos\varphi = 0.66$, 5.6% gain) but is superseded by CrVD topology (TPV = 35.4 Nm/dm^3, $\cos\varphi = 0.67$, 9% gain).

Even better performance results are achieved by standard Zh (TPV = 36.2 Nm/dm^3, 11.4% gain) and MZhED topology (TPV = 36.4 Nm/dm^3, 12.1% gain) but without any power factor increase ($\cos\varphi = 0.67$). Finally, the best result is obtained by MZhVD topology with full barrier depth variance (TPV = 37.3 Nm/dm^3, $\cos\varphi = 0.69$, 14.9% gain). All designs fulfill the structural integrity constraint (FOS ≥ 2). Corresponding torque-speed curves for the studied topologies are shown on Figure 13.

The maximization of torque per volume (TPV $= T_{avg}/V_{active}$) leads to maximization of average torque and minimization of active volume. In this case, stator diameter is fixed meaning that stack length will be minimal ($l_s = 180$ mm, Table 5). Average torque maximization should always be considered together with torque ripple. Both are obtained by running a transient calculation which is a standard time-stepping simulation where the position of the rotor changes place synchronously in time with stator magnetomotive force. Transient simulation is a computationally expensive part of the design evaluation and depending on required details can take several minutes.

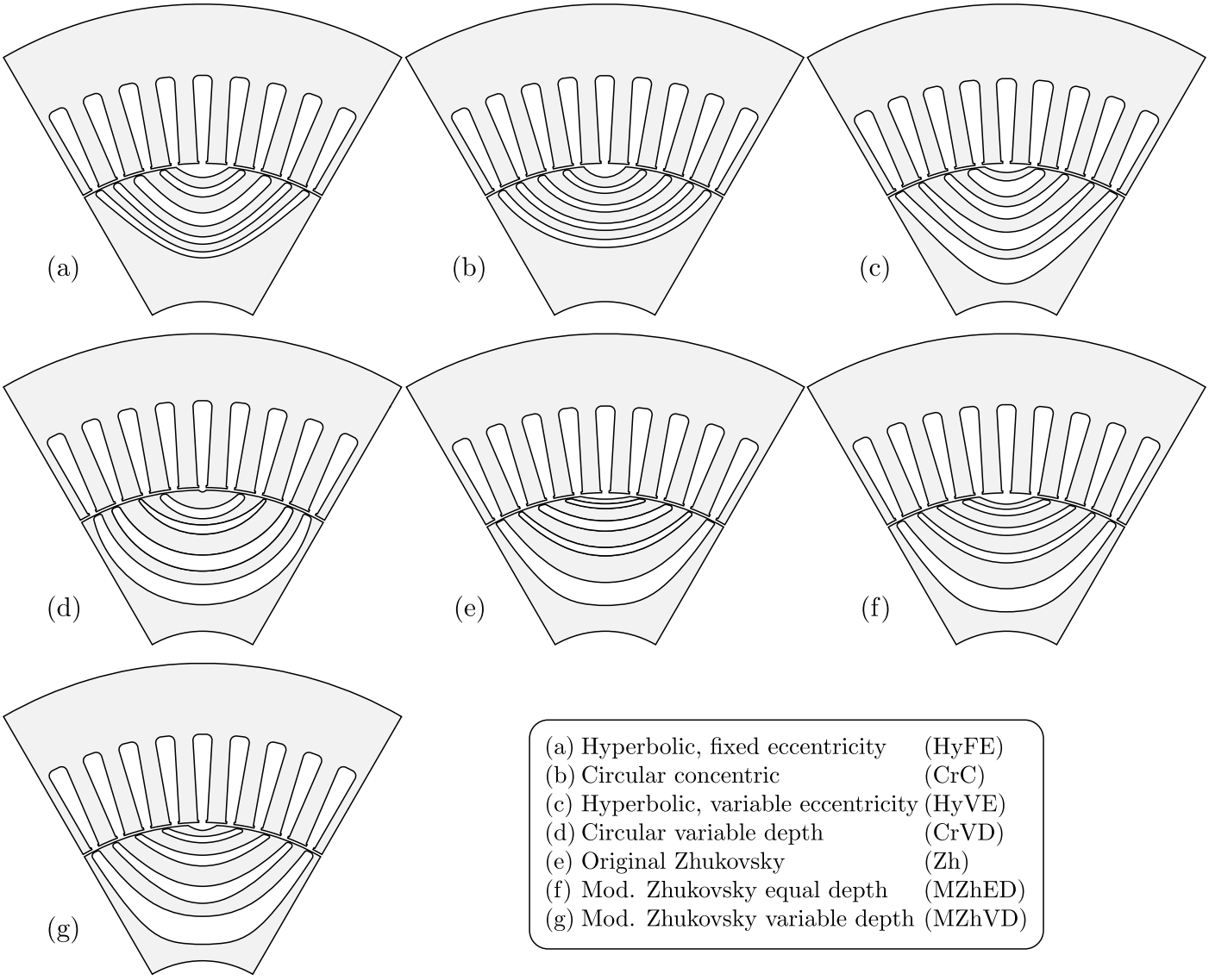

Figure 14. Optimized cross sections per topology.

Table 6. List of all optimized parameters for design variants with $k = 4$.

No:	Description	Symbol	Zh	MZhED	HyFE	CrC	MZhVD	HyVE	CrVD	Unit
1	Stator diameter	D_s	214	214	214	214	214	214	214	mm
2	Shaft diameter	D_{sh}	54	54	54	54	54	54	54	mm
3	Phase number	N_{ph}	3	3	3	3	3	3	3	-
4	No. of turns	N_c	21	21	21	21	22	21	21	-
5	Parallel paths	a_p	6	6	6	6	6	6	6	-
6	Coil throw	y_c	9	9	9	9	9	9	9	-
7	Barrier number	k	4	4	4	4	4	4	4	-
8	Pole pairs	p	3	3	3	3	3	3	3	-
9	Slot number	N_s	54	54	54	54	54	54	54	-
10	Barrier bridge	w_{bb}	0.3	0.3	0.3	0.3	0.3	0.3	0.3	mm
11	Airgap	δ	0.7	0.7	0.7	0.7	0.7	0.7	0.7	mm
12	Slot opening	w_{op}	2	2	2	2	2	2	2	mm
13	Fill factor	-	0.43	0.43	0.43	0.43	0.43	0.43	0.43	-
14	Tooth tip depth	d_t	0.5	0.5	0.5	0.5	0.5	0.5	0.5	mm
15	Point$_1$ inner angle	$\vartheta_{1_{\mathrm{in}}}$	0.35	0.42	0.35	0.35	0.35	0.35	0.46	-
16	Point$_1$ outer angle	$\vartheta_{1_{\mathrm{out}}}$	0.00	0.00	0.00	0.00	0.00	0.00	0.00	-
17	Point$_2$ inner angle	$\vartheta_{2_{\mathrm{in}}}$	0.40	0.33	0.46	0.36	0.29	0.12	0.25	-
18	Point$_2$ outer angle	$\vartheta_{2_{\mathrm{out}}}$	0.00	-0.04	0.06	0.01	0.00	0.00	0.06	-
19	Point$_3$ inner angle	$\vartheta_{3_{\mathrm{in}}}$	0.12	0.13	0.25	0.24	0.18	0.24	0.14	-
20	Point$_3$ outer angle	$\vartheta_{3_{\mathrm{out}}}$	0.09	0.09	0.09	0.09	0.09	0.09	0.09	-
21	Point$_4$ inner angle	$\vartheta_{4_{\mathrm{in}}}$	0.00	0.00	0.00	0.00	0.00	0.00	0.00	-
22	Point$_4$ outer angle	$\vartheta_{4_{\mathrm{out}}}$	0.35	0.35	0.35	0.35	0.35	0.35	0.35	-
23	Corner radius$_1$ inner	$r_{1_{\mathrm{in}}}$	0.89	0.90	0.94	0.90	0.91	0.90	0.89	-
24	Corner radius$_1$ outer	$r_{1_{\mathrm{out}}}$	0.90	0.90	0.89	0.88	0.89	0.90	0.91	-
25	Corner radius$_2$ inner	$r_{2_{\mathrm{in}}}$	0.88	0.16	0.90	0.90	0.50	0.90	0.90	-
26	Corner radius$_2$ outer	$r_{2_{\mathrm{out}}}$	0.87	0.90	0.90	0.55	0.90	0.99	0.90	-
27	Corner radius$_3$ inner	$r_{3_{\mathrm{in}}}$	0.88	0.89	0.90	0.89	0.90	0.88	0.89	-
28	Corner radius$_3$ outer	$r_{3_{\mathrm{out}}}$	0.90	0.90	0.90	0.90	0.90	0.90	0.90	-
29	Corner radius$_4$ inner	$r_{4_{\mathrm{in}}}$	0.02	0.85	0.73	0.99	0.95	0.89	0.49	-
30	Corner radius$_4$ outer	$r_{4_{\mathrm{out}}}$	0.20	0.77	0.74	0.85	0.63	0.54	0.20	-
31	Slot corner radius	r_{sc}	0.62	0,61	0.63	0.62	0.59	0.61	0.63	-
32	Slot depth ratio	$\frac{D_s - D_b}{2}$	0.48	0.45	0.46	0.50	0.46	0.46	0.46	-
33	Split ratio	D_s / D_b	0.67	0.72	0.61	0.72	0.67	0.66	0.61	-
34	Active length	l_{s}	180	180	180	180	180	180	180	mm
35	Tooth tip angle	α_t	9.45	9.48	9.49	9.50	9.48	9.47	9.49	○
36	Tooth width ratio	$\frac{D_b \pi}{N_s} - w_{op}$	0.88	0.82	0.78	0.87	0.71	0.84	0.78	-
37	Min. angle	ϑ_{min}	0.14	0.16	0.16	0.15	0.15	0.15	0.12	-
38	Max. angle	ϑ_{max}	0.48	0.49	0.48	0.48	0.50	0.47	0.50	-
39	Notch angle	ϑ_{n}	0.72	0.73	0.71	0.59	0.42	0.10	0.75	-
40	Current density	J	17	17	17	17	17	17	17	A/mm^2
41	Barrier depth$_1$	$D_{1_{\mathrm{in}}}$	-	0.90	0.67	0.80	0.70	0.40	0.40	-
42	Barrier depth$_2$	$D_{2_{\mathrm{in}}}$	-	0.90	0.67	0.80	0.48	0.59	0.39	-
43	Barrier depth$_3$	$D_{3_{\mathrm{in}}}$	-	0.90	0.67	0.80	0.48	0.43	0.42	-
44	Barrier depth$_4$	$D_{4_{\mathrm{in}}}$	-	0.90	0.67	0.80	0.71	0.60	0.63	-
45	Barrier depth$_1$	$D_{1_{\mathrm{out}}}$	-	0.90	0.67	0.80	0.80	0.40	0.64	-
46	Barrier depth$_2$	$D_{2_{\mathrm{out}}}$	-	0.90	0.67	0.80	0.81	0.53	0.79	-
47	Barrier depth$_3$	$D_{3_{\mathrm{out}}}$	-	0.90	0.67	0.80	0.79	0.68	0.79	-
48	Barrier depth$_4$	$D_{4_{\mathrm{out}}}$	-	0.90	0.67	0.80	0.92	0.80	0.42	-
49	Notch depth	D_n	-	0.90	0.67	0.80	0.60	0.50	0.50	-

4.2. Torque Ripple Mitigation

One of the inherent disadvantages of the SyRM is the increased torque ripple. The issue can be mitigated with the use of asymmetric rotor poles [17,19] or with rotor or stator skewing [40,41]. The drawback of using skewing in optimization is a prolonged transient calculation (it has to be done for each of the rotor slices, e.g., 5 segment rotor skew will have 5 times longer transient simulation). Additionally, the PTO shaft has historically been a part of the Diesel engine which has a quite big ripple [3,4], so the decision was made to optimize the e-PTO machine without skewing.

Typically, SyRM torque ripple is minimized by continuous rotor skewing [40]. The alternatives are segmented rotor skewing or continuous stator skewing. Stator skewing is usually out of scope due to higher production complexity. To illustrate the benefits and drawbacks of the skewing, we have performed post-optimization transient simulation of 5 segment rotor skew (Figure 15b), and continuous rotor skew (Figure 15c). Both approaches yield similar results with a slight advantage to segmented rotor skewing. Since continuous skewing leads to increased manufacturing costs, a segmented skewing of the rotor might also be a good choice [41]. Note that torque ripple for all topologies is less than 15% which is a good feature for a non-skewed SyRM (Figure 15a). The total skew is $360/54 = 6.66°$ mech. (angle of one stator slot).

Note that skewing reduces both the average torque by approx. 3–4%, and torque ripple to approx. 2–5% depending on the topology.

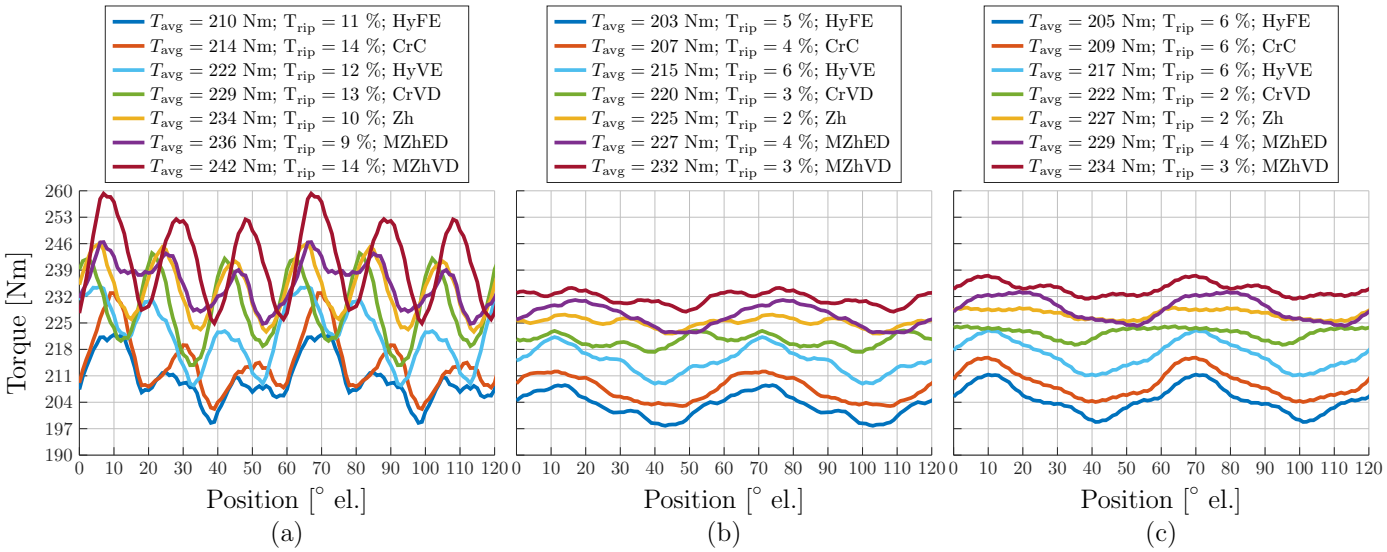

Figure 15. (**a**) Transient torque without skewing; (**b**) Transient torque with 5 segment rotor skewing; (**c**) Continuous skewing.

4.3. Barrier Number Considerations

The purpose of rotor barriers is to create magnetic anisotropy and achieve a high inductance saliency ratio (5), thus producing a high reluctance torque component (6). Simplified, more rotor barriers with an appropriate combination of poles and stator slots should correspond to higher electromagnetic torque.

According to [42,43], the golden rule of barrier number selection is given in the (7). The same approach was used in this paper leading to $k \leq 54/4/3 \leq 4.5 \rightarrow k = 4$. Other combinations of barrier numbers and stator slots might lead to increased torque ripple and decreased performance.

$$\xi = L_d / L_q \tag{5}$$

$$T_{em} = \frac{3}{2} p (L_d - L_q) i_q i_d \tag{6}$$

$$k \leq N_s / (4p) \tag{7}$$

To confirm that $k = 4$ is the proper number of barrier layers, a separate optimization for k = 3–5 was performed on the best barrier type (MZhVD), with equal performance requirements and design selection method as in the previous sections.

Figure 16 shows the Pareto fronts of the optimized designs (results listed in Table 7). It is apparent that three-layer topology is sub-optimal compared with k = 4, 5. In this case, three-layer topology is considered the baseline design. Performance gain is calculated via: Gain $= (T_{\text{avg}}/T_{\text{MZhVD k=3 avg}} - 1) \cdot 100\%$.

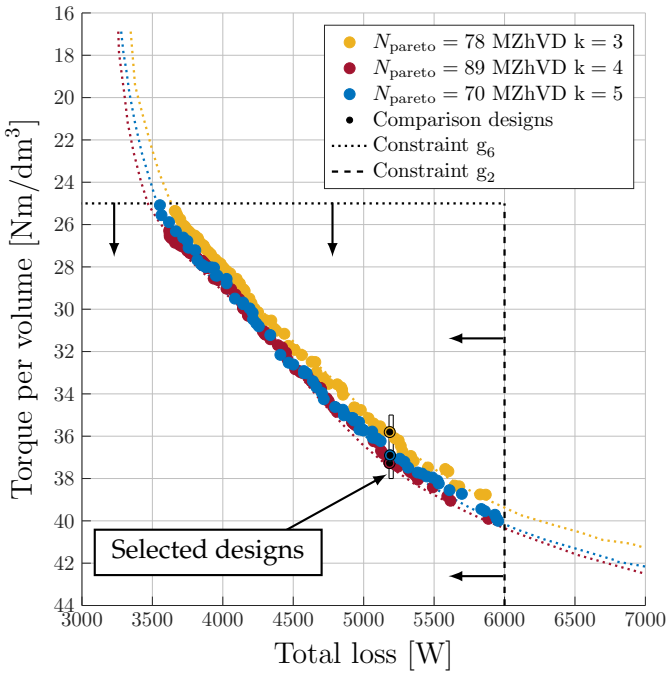

Figure 16. Validated MZhVD Pareto front for k = 3–5 within constraints g_2 and g_6. Dotted colored lines represent estimated Pareto fronts. N_{pareto} is the number of designs placed on each front.

Table 7. Comparison table of MZhVD topology performance for k = 3–5.

Name	Unit	$k = 3$	$k = 4$	$k = 5$
TPV	Nm/dm^3	35.8	37.3	36.9
V_{active}	dm^3	6.47	6.47	6.47
P_{loss}	kW	5184.84	5184	5187
P_{mech}	kW	41.3	43.0	42.5
T_{avg}	Nm	231.8	241.3	238.9
$T_{\text{ripp.}}$	%	15.3	13.7	13.2
n	rpm	1700	1700	1700
$B_{\text{sy,max}}$	T	1.59	1.56	1.56
$B_{\text{st,max}}$	T	1.87	1.84	1.83
FOS	-	2.6	6.3	2.0
m	kg	43.2	44.1	44.0
THL	MA^2/m^3	1.43	1.52	1.45
l_s	mm	180	180	180
γ	○	62.2	62.9	63.2
I_{max}	A$_{\text{rms}}$	89.7	95.7	91.5
cos φ	-	0.70	0.69	0.70
η	%	88.8	89.2	89.1
Gain	%	0.0	4.1	3.1

Compared with the three-layer variant, k = 4 yields the highest performance gain (4.1%) while k = 5 results in 3.1% gain. Furthermore, the three-layer variant results in a

higher torque ripple (15.3%) while k = 4, 5 has approximately the same ripple (13.7% and 13.2% respectively).

An additional parameter in favor of k = 4 is a mechanical factor of safety (FOS = 6.3). Three barrier layers reduce FOS to 2.6 (the reduction accrues due to more steel in the rotor structure), while k = 5 has borderline FOS = 2 due to the more air barriers at a reduced amount of steel in the rotor structure.

Considering that k = 4 is performance wise better than $k = 3, 5$, the comparison confirms that the original barrier number selection was the appropriate choice (all optimized cross sections are listed in Figure 17.

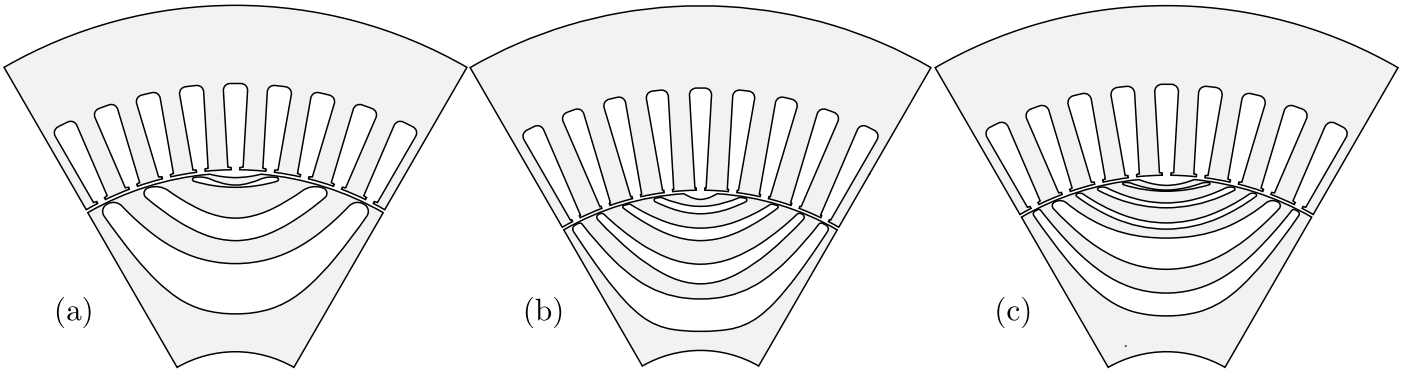

Figure 17. Optimized cross sections of MZhVD topology; (**a**) k = 3; (**b**) k = 4; (**c**) k = 5.

4.4. Execution Time and Computational Cost

The entire optimization process was conducted on a computing workstation with 4 core Intel Core i7 central processing unit (CPU). Execution time of the entire study is summarized in Table 8. The number of CPU cores is important because it enables parallel computing during sensitivity analysis and Pareto front validation (more cores results in shorter overall execution time). The selected number of designs for sensitivity analysis (variation study) of each design variant is $N_{\mathrm{Dsg}} = 300$.

Table 8. Execution time comparison for the entire study.

Stage		Avg. Design Eval. Time	Sensitivity Analysis	MOP Building	OSL Optimization	Pareto Validation	Total Execution Time	Total Execution Time
Type	***k***	**[s]**	**[min]**	**[min]**	**[min]**	**[min]**	**[min]**	**[h]**
Zh	4	55.02	114.6	211.0	11.7	45.9	383.2	6.39
MZhED	4	55.60	115.8	218.9	12.2	46.3	393.2	6.55
MZhVD	3	55.89	116.4	232.0	12.9	46.6	407.9	6.80
HyFE	4	56.30	117.3	249.8	13.9	46.9	427.9	7.13
CrC	4	57.20	119.2	248.5	13.8	47.7	429.1	7.15
MZhVD	4	58.30	121.5	246.6	13.7	48.6	430.3	7.17
HyVE	4	58.20	121.3	248.6	13.8	48.5	432.2	7.20
CrVD	4	58.40	121.7	249.4	13.9	48.7	433.6	7.23
MZhVD	5	60.50	126.0	261.2	14.5	50.4	452.2	7.54

Total sensitivity analysis time mainly depends on the average design evaluation time of a particular topology, which is a function of parametric topology complexity and FEA tool procedures (e.g., adaptive meshing density). It is important to note that the average design execution time for all variants is in the range of 55–61 s, which results in a total sensitivity analysis time of 114–126 min. The building of surrogate models (MOP) is purely a function of the parametric complexity of each topology which varies in a range of 211 min (Zh, k = 4) for the simplest, to 261 min for the most complex topology (MZhVD, k = 5). OSL optimization is the shortest component which takes approximately 12 min. Next, Pareto

front validation is conducted on $N_{\mathrm{Par}} = 200$ designs. This step is effectively the same as in the sensitivity analysis, and the execution time solely depends on the average design evaluation time and N_{Par}.

Finally, the total execution time is summarized based on all previous steps. It varies from 6.39 h (Zh, $k = 4$) to 7.54 h (MZhVD, $k = 4$).

Without the use of the proposed meta-modeling procedure, the total execution time with the same level of details would take several weeks. On the other hand, the total execution time for the entire study (9 investigated topologies) is 63.2 h.

4.5. Efficiency Consideration

Automotive applications are characterized by variable load. Considering that e-PTO load is quite intermittent ([3], e.g., refuse compression, hook-lift loading...), in correspondence with the automotive company which partially sponsored the presented research, it was decided to design the SyRM for peak load operation (maximum current at base speed).

By analyzing the efficiency of the best topology (MZhVD) at the base speed (Table 5), one might conclude that the efficiency is quite low (89.2%). On the other hand, considering that the machine is optimized for peak operation (temporary overload condition), seemingly low efficiency is expected behavior. A more detailed analysis of the entire efficiency map reveals higher efficiency values (Figure 18). Typically water cooled e-PTO machine has a continuous torque envelope of approx. 50% of the max torque (dashed line on Figure 18) yielding 92% efficiency at base speed. Furthermore, if e-PTO hydraulic pump is selected for the max. efficiency area (2400 rpm), efficiency increases to 94%. In case efficiency is still unsatisfactory, changing lamination to higher grade magnetic steel can easily push the efficiency to the premium range [25].

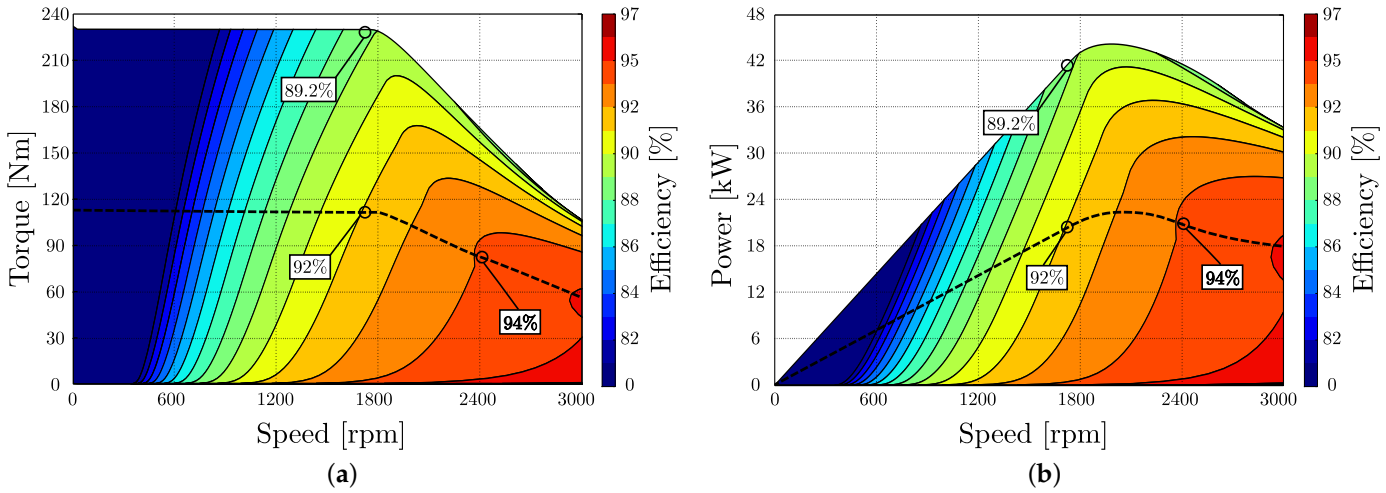

Figure 18. MZhVD efficiency relative to the (**a**) torque-speed and (**b**) power-speed characteristic.

5. Conclusions

Nowadays, due to the confidence in FEA modeling, and rapid product iteration (especially in the automotive sector), electric machine designers primarily rely on simulations. This approach reduces time and cost and is very useful when comparing different machine topologies. Considering that prototyping comes in later project stages, no machines have been produced and tested. Nevertheless, considering that the presented tool chain (Matlab, Motor-CAD, and OptiSlang) is widely used in the automotive industry, we are confident that the results are highly relevant.

As expected, the SyRM rotor barrier topology substantially affects the final machine performance. The consequence of barrier depth variation is variable flux carrier thickness, which has a positive impact on performance and mechanical integrity.

Seven six-pole rotor topologies have been derived from standard barrier types. Simple variants (HyFE, CrC) have the worst performance; more complex designs with limited flux

carrier variation (HyVE, CrVD) yield slight improvement. Better results (but without any power factor increase) are achieved by Zh and MZhED. The best performance and a power factor increase are achieved by a novel MZhVD topology.

The novelty of the proposed approach reflects in the systematic comparison of different "smooth barrier" SyRM topologies via metamodel-based optimization. This offers a fair topology comparison and finally proves that modified Zhukowsky-based topologies yield the best results in terms of TPV and higher power factor.

We want to emphasize that the goal of the paper is to present the novel metamodel based optimization method, and the comparison of SyRM rotor barrier types. This was successfully shown in the case of the e-PTO motor. All design variants are optimized on equal terms, which gives us confidence in the results. Since the conflicting optimization objectives were maximizing TPV and minimization of losses, we are strongly convinced that equal results in barrier performance differences would appear if a different application example was selected. Therefore, the specifics of the e-PTO application and the selected Pareto front combinations of TPV vs. total loss do not limit the performance of the method and do not limit the generality of the method.

Furthermore, the presented machines are optimized for short-term maximum load, which was determined as a critical e-PTO function. The main motivation for the project was to minimize the cost of the machine. Reduced SyRM mass will increase the vehicle range, while the shorter axial length and cheaper stator/rotor steel contribute to the production cost savings. Machine efficiency has not been considered an optimization objective due to the specific use scenario. If higher grade magnetic steel is selected, the efficiency would increase.

Several follow-up projects are planned to be derived from the presented work:

1. Asymmetric rotor topologies with the purpose of torque ripple reduction without skewing.
2. Torque ripple mitigation methods based on non-uniform rotor skew angles and variable segment lengths.
3. Algorithm for the addition of precise corner fillets to arbitrary poly-line curves.

Author Contributions: Conceptualization, B.B.; methodology, B.B. and S.S.; validation, B.B. and S.S.; original draft preparation, B.B.; review and editing, S.S.; visualization, B.B.; supervision, S.S.; funding acquisition, S.S. All authors have read and agreed to the published version of the manuscript.

Funding: This work was partially supported by the Croatian Science Foundation under the project IP-2018-01-5822-HYDREL.

Institutional Review Board Statement: Not applicable.

Informed Consent Statement: Not applicable.

Data Availability Statement: Not applicable.

Acknowledgments: This paper is an extension of Branko Ban's Ph.D. research work on Synchronous Reluctance machines mentored by Stjepan Stipetic.

Conflicts of Interest: The authors declare no conflict of interest.

Abbreviations

The following abbreviations are used in this manuscript:

Abbreviation	Description
ASKA	Adaptive-Sampling Kriging Algorithm
CoP	Coefficient of prognosis
CPU	Central processing unit
CrC	Circular concentric barrier
CrVD	Circular variable depth barrier
DE	Differential evolution
e-PTO	Electric power take off
EV	Electric vehicle
FEA	Finite element analysis
GA	Genetic algorithm
HyFE	Hyperbolic fixed eccentricity barrier
HyVE	Hyperbolic variable eccentricity barrier
IM	Induction machine
IPM	Interior permanent magnet
MOP	Model of prognosis
MTPA	Maximum torque per Ampere
MZhED	Modified Zhukovsky equal depth barrier
MZhVD	Modified Zhukovsky variable depth barrier
NGnet	Normalized Gaussian network
OA	Optimization algorithm
OSL	OptiSlang
PM	Permanent magnet
PTO	Power take off
SyRM	Synchronous reluctance machine
TPV	Torque per volume
THL	Thermal loading coefficient
Zh	Original Zhukovsky barrier

References

1. Murataliyev, M.; Degano, M.; Nardo, M.D.; Bianchi, N.; Gerada, C. Synchronous Reluctance Machines: A Comprehensive Review and Technology Comparison. *Proc. IEEE* **2022**, *110*, 382–399.
2. Ban, B.; Stipetic, S.; Klanac, M. Synchronous reluctance machines: Theory, design and the potential Use in traction applications. In Proceedings of the International Conference on Electrical Drives and Power Electronics, High Tatras, Slovakia, 24–26 September 2019; pp. 177–188.
3. Ban, B.; Stipetić, S. Electric Multipurpose Vehicle Power Take-Off: Overview, Load Cycles and Actuation via Synchronous Reluctance Machine. In Proceedings of the International Aegean Conference on Electrical Machines and Power Electronics (ACEMP-OPTIM), Istanbul, Turkey, 27–29 August 2019.
4. Ban, B.; Stipetic, S. Design and optimization of synchronous reluctance machine for actuation of electric multi-purpose vehicle power take-off. In Proceedings of the 2020 International Conference on Electrical Machines, (ICEM 2020), Online, 23–26 March 2020; pp. 1750–1757.
5. Lampinen, J. Multi-Constrained Nonlinear Optimization by the Differential Evolution Algorithm. In *Soft Computing and Industry*; Springer: London, UK, 2002.
6. Zarko, D. A Systematic Approach to Optimized Design of Permanent Magnet Motors with Reduced Torque Pulsations. Ph.D. Thesis, University of Wisconsin, Madison, WI, USA, 2004.
7. Stipetic, S.; Miebach, W.; Zarko, D. Optimization in design of electric machines: Methodology and workflow. In Proceedings of the Joint International Conference-ACEMP 2015: Aegean Conference on Electrical Machines and Power Electronics, OPTIM 2015: Optimization of Electrical and Electronic Equipment and ELECTROMOTION 2015: International Symposium on Advanced Electromechanical Moti, Side, Turkey, 2–4 September 2016; pp. 441–448.
8. Gamba, M.; Pellegrino, G.; Armando, E.; Ferrari, S. Synchronous Reluctance Motor with Concentrated Windings for IE4 Efficiency. In Proceedings of the IEEE Energy Conversion Congress and Exposition (ECCE), Cincinnati, OH, USA, 1–5 October 2017.
9. Calzo, G.L.; Galea, M. Design Optimization of a High-Speed Synchronous Reluctance Machine. *IEEE Trans. Ind. Appl.* **2018**, *54*, 233–243.
10. Babetto, C.; Bacco, G.; Bianchi, N. Synchronous Reluctance Machine Optimization for High-Speed Applications. *IEEE Trans. Energy Convers.* **2018**, *33*, 1266–1273.
11. De Pancorbo, S.M.; Ugalde, G.; Poza, J.; Egea, A. Comparative study between induction motor and Synchronous Reluctance Motor for electrical railway traction applications. In Proceedings of the 5th International Conference on Electric Drives Production, (EDPC 2015), Nuremberg, Germany, 15–16 September 2015; pp. 2–6.

12. Villan, M.; Tursini, M.; Popescu, M.; Fabri, G.; Credo, A.; Di Leonardo, L. Experimental comparison between induction and synchronous reluctance motor-drives. In Proceedings of the 2018 23rd International Conference on Electrical Machines, ICEM 2018, Alexandroupoli, Greece, 3–6 September 2018; pp. 1188–1194.
13. Villani, M. High Performance Electrical Motors for Automotive Applications–Status and Future of Motors with Low Cost Permanent Magnets. Ph.D. Thesis, University of l'Aquila, Aquila, Italy, 2020.
14. Castagnaro, E.; Bianchi, N. *High-Speed Synchronous Reluctance Motor for Electric-Spindle Application*; Institute of Electrical and Electronics Engineers Inc.: Piscataway, NJ, USA, 2020; pp. 2419–2425.
15. Bao, Y.; Degano, M.; Wang, S.; Chuan, L.; Zhang, H.; Xu, Z.; Gerada, C. A Novel Concept of Ribless Synchronous Reluctance Motor for Enhanced Torque Capability. *IEEE Trans. Ind. Electron.* **2020**, *67*, 2553–2563.
16. Credo, A.; Fabri, G.; Villani, M.; Popescu, M. High speed synchronous reluctance motors for electric vehicles: A focus on rotor mechanical design. In Proceedings of the 2019 IEEE International Electric Machines and Drives Conference, (IEMDC 2019), San Diego, CA, USA, 12–15 May 2019; pp. 165–171.
17. Kafadar, A.S.; Tap, A.; Ergene, L.T. Torque ripple reduction of SynRM using machaon type lamination. In Proceedings of the 2018 6th International Conference on Control Engineering and Information Technology, (CEIT 2018), Istanbul, Turkey, 25–27 October 2018; pp. 25–27.
18. Ban, B.; Stipetic, S. Absolutely Feasible Synchronous Reluctance Machine Rotor Barrier Topologies with Minimal Parametric Complexity. *Machines* **2022**, *10*, 206.
19. Ferrari, M.; Bianchi, N.; Doria, A.; Fornasiero, E. Design of Synchronous Reluctance Motor for Hybrid Electric Vehicles. *IEEE Trans. Ind. Appl.* **2015**, *51*, 21–36.
20. Tawfiq, K.B.; Ibrahim, M.N.; El-Kholy, E.E.; Sergeant, P. Performance Improvement of Synchronous Reluctance Machines—A Review Research. *IEEE Trans. Magn.* **2021**, *57*, 99.
21. Varatharajan, A.; Brunelli, D.; Ferrari, S.; Pescetto, P.; Pellegrino, G. *SyreDrive: Automated Sensorless Control Code Generation for Synchronous Reluctance Motor Drives*; Institute of Electrical and Electronics Engineers Inc.: Piscataway, NJ, USA, 2021; pp. 192–197.
22. Tawfiq, K.B.; Ibrahim, M.N.; El-Kholy, E.E.; Sergeant, P. Performance Analysis of a Rewound Multiphase Synchronous Reluctance Machine. *IEEE J. Emerg. Sel. Top. Power Electron.* **2022**, *10*, 297–309.
23. Tawfiq, K.B.; Ibrahim, M.N.; El-Kholy, E.E.; Sergeant, P. Construction of Synchronous Reluctance Machines with Combined Star-Pentagon Configuration Using Standard Three-Phase Stator Frames. *IEEE Trans. Ind. Electron.* **2022**, *69*, 7582–7595.
24. Ibrahim, M.N.F.; Abdel-Khalik, A.S.; Rashad, E.M.; Sergeant, P. An Improved Torque Density Synchronous Reluctance Machine with a Combined Star-Delta Winding Layout. *IEEE Trans. Energy Convers.* **2018**, *33*, 1015–1024.
25. Ibrahim, M.N.; Sergeant, P.; Rashad, E.M. Synchronous Reluctance Motor Performance Based on Different Electrical Steel Grades. *IEEE Trans. Magn.* **2015**, *51*, 7403304.
26. Mirazimi, M.S.; Kiyoumarsi, A. Magnetic Field Analysis of Multi-Flux-Barrier Interior Permanent-Magnet Motors Through Conformal Mapping. *IEEE Trans. Magn.* **2017**, *53*, 7002512.
27. Mirazimi, M.S.; Kiyoumarsi, A. Magnetic Field Analysis of SynRel and PMASynRel Machines with Hyperbolic Flux Barriers Using Conformal Mapping. *IEEE Trans. Transp. Electrif.* **2020**, *6*, 52–61.
28. Taghavi, S.; Pillay, P. Design aspects of a 50hp 6-pole synchronous reluctance motor for electrified powertrain applications. In Proceedings of the IECON 2017—43rd Annual Conference of the IEEE Industrial Electronics Society, Beijing, China, 29 October–1 November 2017; pp. 2252–2257.
29. Gamba, M.; Pellegrino, G.; Cupertino, F. Optimal number of rotor parameters for the automatic design of Synchronous Reluctance machines. In Proceedings of the 2014 International Conference on Electrical Machines, ICEM 2014, Berlin, Germany, 9 February 2014; pp. 1334–1340.
30. Cupertino, F.; Pellegrino, G.; Cagnetta, P.; Ferrari, S.; Perta, M. SyRE: Synchronous Reluctance (Machines)-Evolution, 2021.
31. Kamper, M.J.; Van Der Merwe, F.S.; Williamson, S. Direct Finite Element Design Optimisation of the Cageless Reluctance Synchronous Machine. *IEEE Trans. Energy Convers.* **1996**, *11*, 547–553.
32. Gundogdu, T.; Komurgoz, G. A systematic design optimization approach for interior permanent magnet machines equipped with novel semi-overlapping windings. *Struct. Multidiscip. Optim.* **2021**, *63*, 1491–1512.
33. Lee, J.; Seo, J.H.; Kikuchi, N. Topology optimization of switched reluctance motors for the desired torque profile. *Struct. Multidiscip. Optim.* **2010**, *42*, 783–796.
34. Lee, C.; Jang, I.G. Topology optimization of multiple-barrier synchronous reluctance motors with initial random hollow circles. *Struct. Multidiscip. Optim.* **2021**, *64*, 2213–2224.
35. Otomo, Y.; Igarashi, H. Topology Optimization Using Gabor Filter: Application to Synchronous Reluctance Motor. *IEEE Trans. Magn.* **2021**, *9464*, 18–21.
36. Bramerdorfer, G.; Zăvoianu, A.C. Surrogate-Based Multi-Objective Optimization of Electrical Machine Designs Facilitating Tolerance Analysis. *IEEE Trans. Magn.* **2017**, *53*, 1–11.
37. Son, J.c.; Ahn, J.m.; Lim, J. Optimal Design of PMa-SynRM for Electric Vehicles Exploiting Adaptive-Sampling Kriging Algorithm. *IEEE Access* **2021**, *9*, 41174–41183.
38. Riviere, N.; Volpe, G.; Villani, M.; Fabri, G.; Di Leonardo, L.; Popescu, M. Design analysis of a high speed copper rotor induction motor for a traction application. In Proceedings of the 2019 IEEE International Electric Machines and Drives Conference, (IEMDC 2019), San Diego, CA, USA, 12–15 May 2019.

39. Stipetic, S.; Zarko, D.; Popescu, M. Ultra-fast axial and radial scaling of synchronous permanent magnet machines. *IET Electr. Power Appl.* **2016**, *10*, 658–666.
40. Bomela, X.B.; Kamper, M.J. Effect of stator chording and rotor skewing on performance of reluctance synchronous machine. *IEEE Trans. Ind. Appl.* **2002**, *38*, 91–100.
41. Hubert, T.; Reinlein, M.; Kremser, A.; Herzog, H.G. Torque ripple minimization of reluctance synchronous machines by continuous and discrete rotor skewing. In Proceedings of the 2015 5th International Conference on Electric Drives Production, (EDPC 2015), Nuremberg, Germany, 15–16 September 2015.
42. Pellegrino, G. Permanent Magnet Machine Design and Analysis with a Focus to Flux-switching PM and PM-assisted Synchronous Reluctance Machines Part II: PM-assisted Synch Rel Machines Tutorials. In Proceedings of the 2016 International Conference on Electrical Machines, (ICEM 2016), Lausanne, Switzerland, 4–7 September 2016.
43. Vagati, A.; Pastorelli, M.; Franceschini, G.; Petrache, S.C. Design of low-torque-ripple synchronous reluctance motors. *IEEE Trans. Ind. Appl.* **1998**, *34*, 758–765.